Towards photo-CIDNP MAS NMR as a generally applicable enhancement method

Thamarath Surendran, S.

Chapter 3

Electron spin density distribution in the special pair triplet of Rhodobacter sphaeroides R26 revealed by the magnetic field dependence of the solid-state photo-CIDNP effect

---

3.1 *Abstract*

Photo-CIDNP (photochemically induced dynamic nuclear polarization) can be observed in frozen and quinone-blocked photosynthetic reaction centers (RCs) as a modification of the magic-angle spinning (MAS) NMR signal intensity upon illumination. Studying the carotenoid-less mutant strain R26 of *Rhodobacter (Rb.) sphaeroides*, experiment and theory provide converging evidence that contributions to the nuclear spin polarization from the three-spin mixing and differential decay mechanisms can be separated from polarization generated by the radical pair mechanism that is due to differential relaxation (DR) between the singlet and triplet branches. In a magnetic field of 1.4 T, the DR contribution leads to dramatic signal enhancement of about 80,000 and dominates over the two other mechanisms. The DR mechanism encodes information on the spin density distribution in the donor triplet state. Relative peak intensities in the photo-CIDNP spectra provide a critical test for triplet spin densities computed for different model chemistries and conformations. The unpaired electrons are distributed almost evenly over the two moieties of the special pair of bacteriochlorophylls, with only slight excess on the P_L half.

This chapter is published in *J. Am. Chem. Soc.* **2012**, *134*, 5921–5930.

3.2 *Introduction*

The solid-state photo-CIDNP effect at high fields, discovered by M. Zysmilich and A. McDermott in 1994 on quinone-reduced and frozen photosynthetic reaction centers,[1] provides a method to overcome the intrinsically low sensitivity of NMR by generation of non-Boltzmann populations of nuclear spin states by photochemical reactions in solids (for review, see 2,3). This photochemically induced dynamic nuclear polarization (photo-CIDNP) can be detected by magic-angle spinning (MAS) NMR as strong modifications of signal intensities. Enhancement factors of more than 10,000 have been reported for ^{13}C photo-CIDNP MAS NMR in a magnetic field of 4.7 T (*i.e.*, 200 MHz ^{1}H frequency and 50 MHz ^{13}C frequency) in photosynthetic reaction centers (RCs) of the purple bacteria *Rhodobacter (Rb.) sphaeroides* wild type (WT)[4] and the carotenoid-less mutant R26.[5] Such strong signal enhancement allows, for example, for highly selective observation of the photosynthetic cofactors at nanomolar concentrations in entire cells.[5,6] Due to the long ^{13}C relaxation time in solids, the nuclear polarization of subsequent photocycles can be accumulated in continuous illumination experiments making photo-CIDNP MAS NMR a sensitive analytical tool. It appears to be an intrinsic property of natural photosynthetic RCs[7-11] and has been proposed to be related to efficient electron transfer.[12] Recently the effect was observed in a blue-light photoreceptor, the phototropin mutant LOV1-C57S at 2.4 T, demonstrating that the effect is not limited to natural photosynthesis (see chapter 4).

The cyclic spin-chemical processes producing such high nuclear polarizations are well understood for a spin-correlated radical pair interacting with a single nuclear spin in the high-field limit in quinone-depleted and quinone-blocked RCs of *Rb. sphaeroides*.[2,13] Upon illumination, RCs of *Rb. sphaeroides*[14,15] form radical pairs with the primary electron donor P, the "special pair" of two bacteriochlorophylls (BChl), as radical cation and the primary electron acceptor Φ, a bacteriopheophytin (BPhe), as radical anion (Scheme 3.1). The initial electron spin zero-quantum coherence, which is created upon photogeneration of the radical pair in the S state in the S-T_0 manifold of states, is transferred by two solid-state mechanisms, the three-spin mixing (TSM)[16,17] and the differential decay (DD),[18] into *net* nuclear polarization. In the electron-electron-nuclear TSM mechanism, the antisymmetry between the α and β nuclear spin states in the singlet and triplet

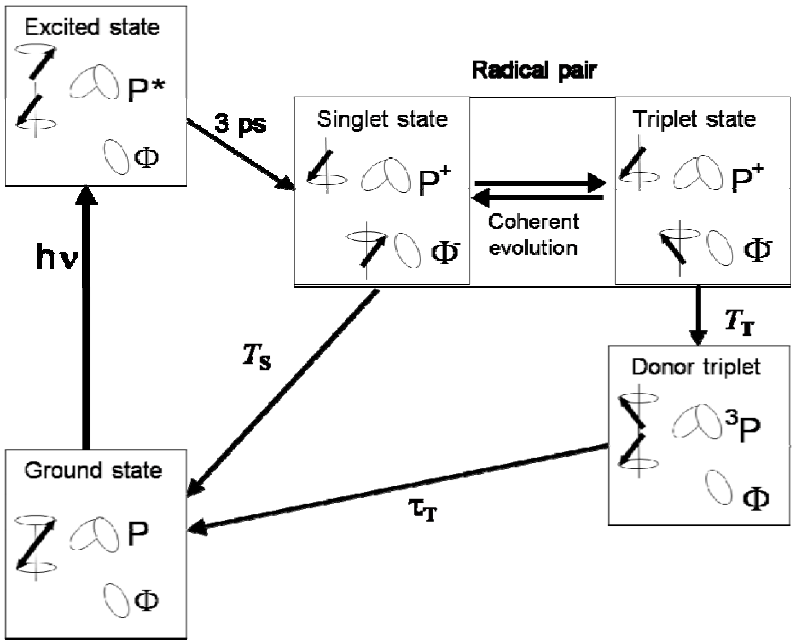

Scheme 3.1. Photocycle in quinone-blocked RCs of *Rb. sphaeroides* WT and R26. Upon illumination and fast electron transfer from an excited singlet state, a radical pair is formed in a pure singlet state having high electron spin order. The radical pair is formed by a radical cation at the two donor BChls (Special pair, P) and a radical anion on the BPhe acceptor cofactor (Φ) of the active branch. The chemical fate of the radical pair depends on its electronic spin state: while the singlet state is allowed to recombine with a lifetime of $T_S = 20$ ns, for the triplet state a direct recombination is spin-forbidden and a donor triplet (^{3}P) is formed by inter-system crossing with a lifetime of $T_T = 1$ ns. The lifetime of ^{3}P depends on the relaxation channel provided by the environment. It is short in WT RCs having a nearby carotenoid and significantly longer in the carotenoid-less mutant R26.

branches during the coherent spin evolution in the correlated radical pair is broken by state mixing due to anisotropic electron-electron dipolar coupling and pseudosecular hyperfine coupling B. The ratio $|\omega_I/A_{zz}|$ determines the extent of mixing of the nuclear spin states, and thus also the extent to which population antisymmetry is violated. State mixing is maximized at the double matching condition $2|\Delta\Omega| = 2|\omega_I| = |A|$, *i.e.*, the difference of the electron Zeeman frequencies $\Delta\Omega$, the nuclear Zeeman frequency ω_I and the secular part of the hyperfine interaction A must match. In the DD mechanism, this antisymmetry of nuclear spin populations is broken by different reaction constants of the decay of the S and the T_0 states (T_S and T_T) of the radical pair as well as by pseudosecular hyperfine coupling B. In this case, only a single matching of interactions $2|\omega_I| = |A|$ is required

and the difference of singlet and triplet radical pair lifetimes must be of the order of the B^{-1}. During the radical pair evolution the occurrence of these two competing mechanisms in RCs of *Rb. sphaeroides* WT leads to a set of entirely emissive (negative) signals, whose relative intensity encodes information on the spin density distribution in the radical pair state.[4] Since $\Delta\Omega$ and ω_I depend on the magnetic field, while A does not, both the TSM and DD mechanism produce maximum absolute nuclear polarization at a matching field.

For RCs having a long donor triplet lifetime, such as the carotenoid-less mutant R26 of *Rb. sphaeroides*, contributions from a third mechanism have been observed.[5] In this situation polarization generated by the radical pair mechanism (RPM),[19,20] which has the same amplitude and opposite sign in the singlet and triplet branch and thus usually cancels in cyclic reactions, is partially maintained[21,22] due to different longitudinal nuclear relaxation in the two branches (for a review see Chapter 1). In the solid state this has been termed the differential relaxation (DR) mechanism to emphasize that RPM polarization is modified according to the different T_1 relaxation rates for different nuclei.[2] This mechanism explains the differences between photo-CIDNP spectra of RCs of *Rb. sphaeroides* WT and R26.[5] The DR mechanism relies on enhanced nuclear relaxation in the triplet branch, which is in turn caused by fluctuations of the anisotropic hyperfine couplings of these nuclei to the donor triplet (^{3}P) in its T_0 state. Therefore, the relative line intensity in this case also encodes information on the spin density distribution in the ^{3}P state.[5] Such information is of interest to understand the photoprotection of the RCs by fast triplet quenching.[14] In addition, studies of the triplet state of bacterial RCs have provided insight into the strongly asymmetric distribution of electron transfer between the nearly symmetric M and L branches of bacterial RCs.[23,24]

In practice, the three mechanisms are operative simultaneously, and for the DR mechanism the relative line intensities depend on the spin density distribution in both the radical pair state (through the RPM) and the donor triplet state (through paramagnetically induced relaxation). In the present work, it is demonstrated that these contributions can be disentangled. The analysis relies on the separate characterization of the RPM polarization by time-resolved ^{13}C photo-CIDNP MAS

NMR[25] and on different field dependences of the three mechanisms. Previous experimental studies on both RC types WT and R26 clearly demonstrated a strong increase of the photo-CIDNP enhancement with lower fields between 17.4 and 4.7 T.[4,5] From the experiment it is not known whether the enhancement further increases and at which field a maximum occurs. The discovery of the effect in a blue-light photoreceptor occurred at an even lower field of 2.4 T (see chapter 4). Simulation of the TSM and DD mechanisms in the high field to medium field range (17.6T to 1.4T) for photosynthetic RCs suggests a maximum polarization at ≈2 T for ^{13}C nuclei,[26] which has not been experimentally verified to date. Although information on the relaxation dispersion of the electron spin in the donor triplet ^3P is restricted, relaxation theory suggests that for the expected electron T_1 spin relaxation times in the microsecond range, paramagnetic relaxation enhancement increases down to fields well below 2 T.[27] Accordingly, DR polarization should dominate at sufficiently low fields. Here, an experimental "trial drill" towards lower fields, as far as commercial NMR hardware allows, is provided. At the fields of 1.4 and 2.4 T, coherent evolution is still strictly within the S-T_0 manifolds, and the contribution of a recently proposed TSM mechanism based on S-T_- mixing[28] appears negligible.

3.3 *Materials and Methods*

3.3.1 *Sample Preparation*

RCs from *Rb. sphaeroides* WT were isolated as described by Shochat *et al.*,[29] RCs from *Rb. sphaeroides* R26 were isolated by the procedure of Feher and Okamura.[30] The removal of Q_A has been done by incubating the RCs at a concentration of 0.6 μM in 4% LDAO, 10 mM *o*-phenanthroline, 10 mM Tris buffer, pH 8.0, for 6 h at 26 ˚C, followed by washing with 0.5 M NaCl in 10 mM Tris buffer, pH 8.0, containing 0.025% LDAO and 1mM EDTA.[31] Approximately 5 mg of the RC protein complex embedded in LDAO micelles was used for NMR measurements.

3.3.2 *MAS-NMR Measurements*

The NMR experiments in different fields were performed with DSX-750, DMX-400, DMX-200, AV-100 and AV-60 NMR spectrometers equipped with MAS probes (Bruker, Karlsruhe, Germany). The sample was loaded into a clear 4-mm sapphire rotor and inserted into the MAS probe. The sample was frozen slowly at a low spinning frequency of ν_r = 400 Hz to ensure a homogenous sample distribution against the rotor wall.[32] The light and dark spectra were collected with a Hahn echo pulse sequence and TPPM proton decoupling.[33] The hardware of the spectrometer does not allow for proton decoupling in magnetic fields less than 2.4 Tesla. The spectra at lower magnetic fields were measured with an anti-ringing pulse sequence.[34] All ^{13}C photo-CIDNP MAS NMR spectra were obtained at a temperature of 235 K with continuous illumination using white light.[35]

The MAS rotation frequency was 8 kHz in all experiments. For the five fields of 1.4, 2.4, 4.7, 9.6 and 17.6 Tesla, line broadenings of 10 Hz, 10 Hz, 20 Hz, 50 Hz or 120 Hz, respectively, were applied prior to the Fourier transformation. In all cases, a cycle delay of 4 s was used. The ^{13}C MAS NMR spectra were referenced to TMS by using the ^{13}COOH response of solid tyrosine·HCl at 172.1 ppm.

3.3.3 *Simulations*

Hyperfine anisotropies ΔA_k in the donor triplet state were computed with ADF 2004.1,[36,37] employing the BLYP functional[38,39] and DP basis sets for ^{13}C nuclei based on the special pair structure from *Rb. sphaeroides* R26 in the charge-neutral state (PDB entry 1AIJ)[40] and with ADF 2009.1[36,41] utilizing a TZP basis set and the BP86 functional.[38,39] The coordinates from the charge-neutral state of *Rb. sphaeroides* WT (PDB entry 1PCR)[42] have been amended with hydrogen atoms and optimized in Turbomole V6.0. For the geometry optimization a TZVP[43] basis and the BP86 functional have been used in combination with the RI approximation using the standard TZVP basis set from Turbomole.[44,45] Coordinates were first optimized for the radical cation state and relaxed in the ^{3}P configuration. DR intensities have been simulated by a home-written Matlab program as described in ref 5, assuming that the nuclear longitudinal relaxation rate constant $1/T_{1n}$ is

proportional to the square of the hyperfine anisotropy ΔA^2 (*vide infra*). Here, ΔA is defined as $3(A_z - a_{iso})/2$, where A_z is the largest eigenvalue of the hyperfine tensor and a_{iso} its trace. Calculation of polarizations for the singlet and triplet branches due to RPM was done by the density operator formalism as described in refs 4 and 5.

3.4 *Results*

Figures 3.1 and 3.2 show the amplitude of the solid-state photo-CIDNP effect in the magnetic field range from 2.4 to 17.6 T in WT and R26, respectively. In this regime, ^{13}C MAS NMR data can be acquired with ^{1}H decoupling. While dark experiments (Figures 3.1 and 3.2, right panel) show an increase in signal intensity and resolution towards higher field, the light-induced signals (Figures 3.1 and 3.2, left panel) show the opposite trend. The lower the field, the stronger the intensity of the light induced signals. The optimum for the spectral resolution is reached at about 4.7 T (200 MHz ^{1}H frequency) since at 2.4 T the spectral dispersion is poor while at higher field artificial line-broadening is required to compensate for low signal-to-noise ratio. In this field range, these trends hold for both types of RCs, WT (Figure 3.1) and R26 (Figure 3.2). Hence, the question arises whether or not the enhancement further increases at even lower field.

Over the entire field range, the intensity patterns are different for the spectra of WT and R26 RCs. While the first provide entirely emissive spectra, for the latter both emissive and absorptive lines occur. Previous analysis has shown that a set of entirely emissive signals originates from both the donor and the acceptor of the primary radical pair of WT RCs (Figure 3.1).[4,13] This non-equilibrium polarization has been interpreted in terms of competing TSM and DD mechanisms.[4] The all-emissive spectrum is caused by a predominance of the TSM over the DD mechanism. For the DD contribution, the sign of the signal depends on the signs of the secular hyperfine coupling and of the *g* tensor difference.[2] In R26 RCs, the DR mechanism leads to admixture of polarization from the RPM for those donor nuclei that exhibit strongly anisotropic hyperfine couplings in the ^{3}P state.[2] For positive isotropic hyperfine couplings in the radical pair state this DR polarization is absorptive, while it is emissive for negative isotropic hyperfine couplings in the

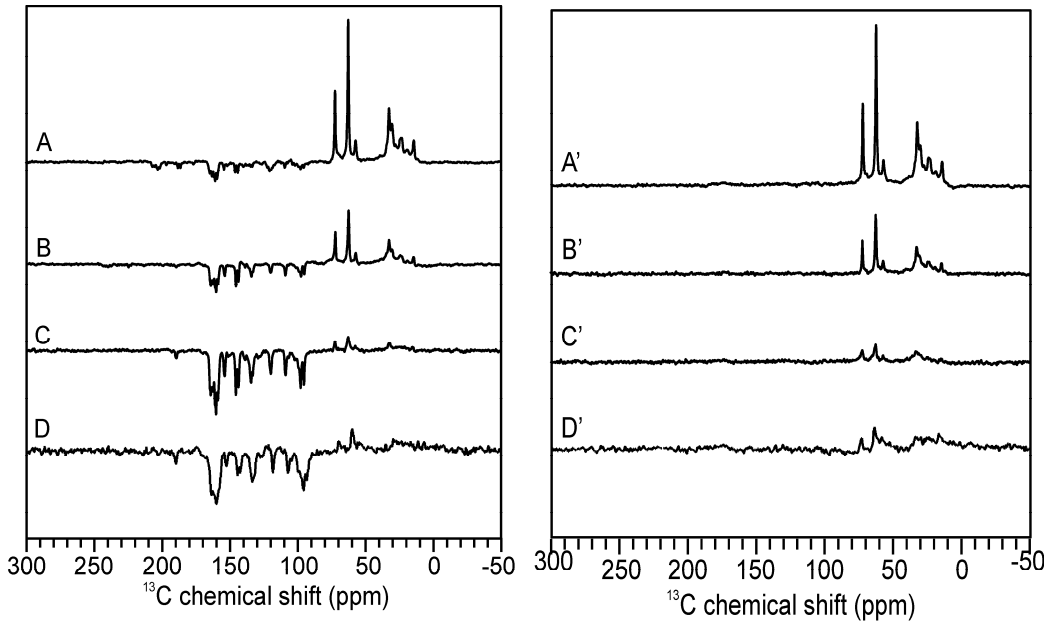

Figure 3.1. ^{13}C MAS NMR spectra of quinone depleted RCs of *Rb. sphaeroides* WT in the dark (right panel) and with illumination (left panel) in a field of 17.6 T (A, A'), 9.4 T (B, B'), 4.7 T (C, C') or 2.4 T (D, D'). The spectra were obtained at 235 K with a MAS frequency of 8 kHz using ^{1}H decoupling.

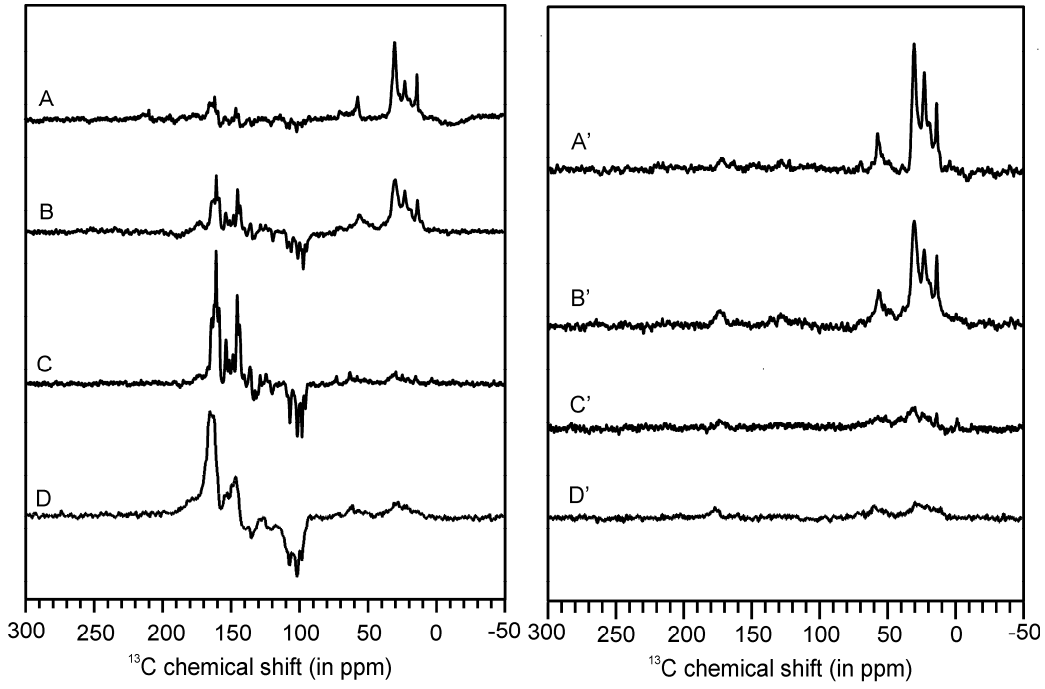

Figure 3.2. ^{13}C MAS NMR spectra of quinone depleted RCs of *Rb. sphaeroides* R26 in the dark (right panel) and with illumination (left panel) in magnetic fields of 17.6 T (A, A'), 9.4 T (B, B'), 4.7 T (C, C') or 2.4 (D, D') T. The spectra were obtained at 235 K with a MAS frequency of 8 kHz using ^{1}H decoupling.

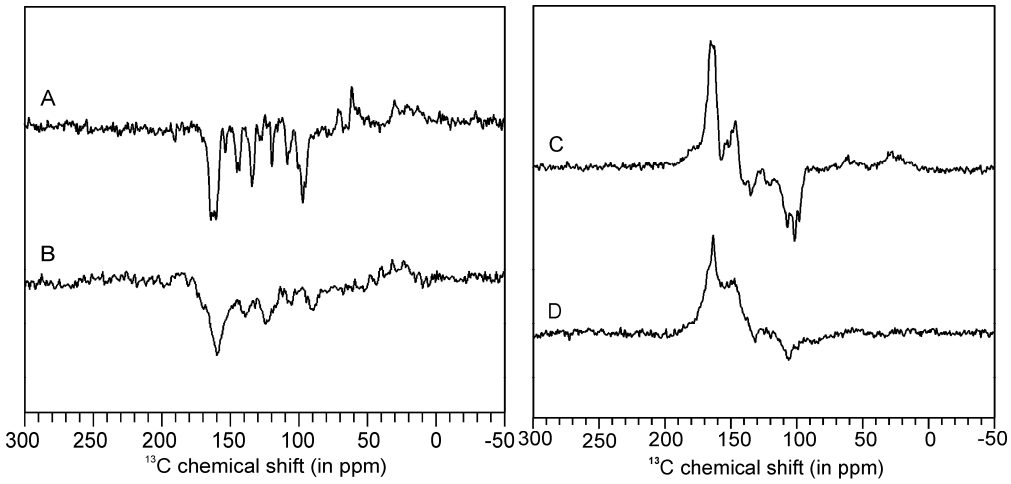

Figure 3.3: ^{13}C photo-CIDNP MAS NMR spectra of *Rb. sphaeroides* WT (left panel) and R26 (right panel) RCs in a magnetic field of 2.4 T with ^{1}H decoupling (A, C) and without ^{1}H decoupling (B, D).

radical pair state. This sign rule may be violated if the anisotropic contribution strongly dominates over the isotropic contribution to the hyperfine coupling in the radical pair state. Generally the field dependence of the TSM, DD, and DR mechanisms may be different, implying that also the spectral pattern changes with the field. In the photo-CIDNP spectra of R26 RCs (Figure 3.2), however, the ratio of negative to positive signals appears to depend only weakly on the field strength.

In magnetic fields less than 2.4 T, our hardware does not allow for ^{1}H decoupling. To compare the effect of decoupling on the spectra, we measured ^{1}H–coupled and decoupled spectra for both samples (Figure 3.3) in a field of 2.4 T. The comparison shows that in particular the signals around 100 ppm, originating from methine bridge carbons that are directly bound to a proton, are broadened beyond detection in the ^{1}H-coupled spectra while the other signals broaden substantially.

Experiments in magnetic fields of 2.4 and 1.4 T (100 and 60 MHz ^{1}H frequency, respectively) for RCs of WT and R26 are shown in Figures 3.4 and 3.5. In Figure 3.4 the solid-state photo-CIDNP effect considerably weakens towards lower fields. Hence, the present data provide empirical evidence that the coherent high-field solid-state photo-CIDNP effect for bacterial RCs shows a maximum around 2.4 T. In Figure 3.5, on the other hand, the light-induced positive feature strongly increases towards lower field. The ratio between positive and negative

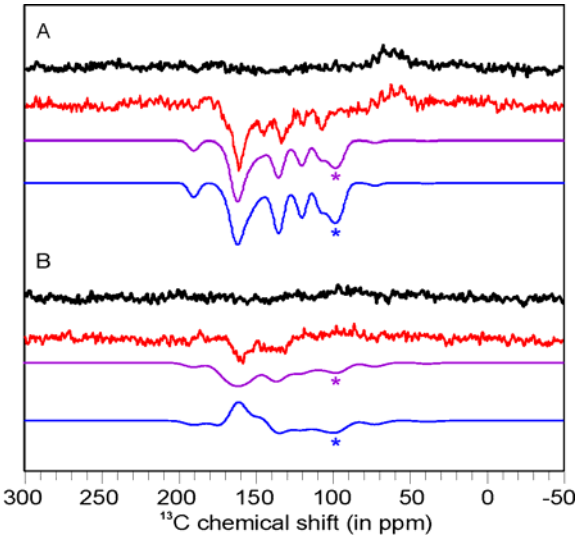

Figure 3.4. ^{13}C MAS NMR spectra of quinone depleted RCs of *Rb. sphaeroides* WT in the dark (black) and with illumination (red), as well as numerical simulations of the photo-CIDNP effect with T_{1T} = 100 ns (lilac) and T_{1T} = 56 ns (blue) at 2.4 Tesla (A) and 1.4 Tesla (B). The experimental data were obtained at a temperature of 235 K with a MAS frequency of 8 kHz and without ^{1}H decoupling. The asterisks mark methine carbon signals that are lost without decoupling.

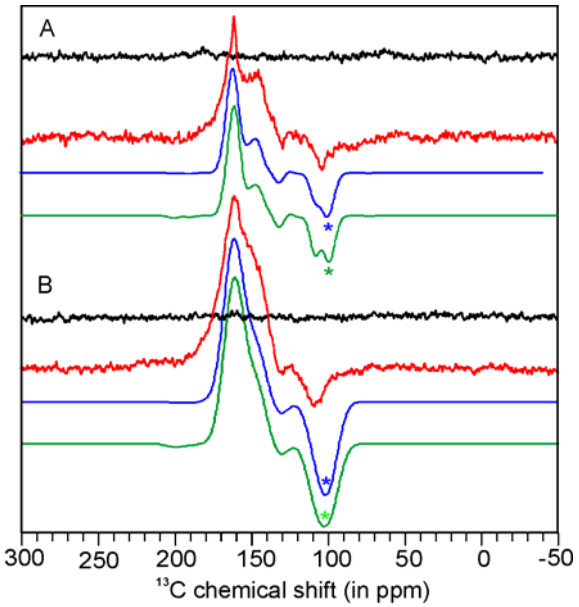

Figure 3.5. ^{13}C MAS NMR spectra of quinone depleted RCs of *Rb. sphaeroides* R26 in the dark (black) and with illumination (red) as well as numerical simulations of the photo-CIDNP effect with T_{1T} = 56 ns and triplet spin density from DFT computations with the BLYP functional (blue) and the BP86 functional (green) in magnetic fields of 2.4 Tesla (A) and 1.4 Tesla (B). The experimental data were obtained at 235 K with a MAS frequency of 8 kHz and without ^{1}H decoupling. The asterisks mark methine carbon signals that are broadened without decoupling.

signals is changed strongly in favor of the first. Thus, while the TSM and DD mechanisms become less efficient at 1.4 T, the DR mechanism becomes more potent. Experiments at even lower fields would require a different type of hardware. In particular, a field cycling system would be suitable to avoid further loss of resolution.

All spectra are presented with similar signal-to-noise ratio. In previous work, using the response of the methyl groups as an internal standard for estimating the enhancement factor of the solid-state photo-CIDNP effect, this factor was found to be about 10000 in a magnetic field of 4.7 T.[4,5] The methyl signal at 30 ppm corresponds to the ~3300 methyl groups in the RC protein. The experiments at 2.4 T for RCs of WT and R26 show stronger enhancement compared to 4.7 T. Using the same standard for the spectra obtained at 2.4 T, enhancement factors have been determined to be 20000 for WT RCs and 40000 for R26 RCs.

Because proton decoupling is not feasible with the spectrometer in our laboratory operating at magnetic fields less than 2.4 T, the enhancement factor cannot be calculated as above. It is, however, possible to estimate the enhancement factor in R26 RCs by comparing with the data collected without proton decoupling at 2.4 and 1.4 T from the same sample in the same measurement time (Figure 3.5 A and B). Since decoupling does not affect the polarization, the factor 40000 is to a reasonable approximation also valid for the spectrum obtained without ^{1}H decoupling. To estimate the polarization, the absorptive and emissive signals are integrated for the spectra of R26 RCs collected in magnetic fields of 2.4 and 1.4 T. The ratio of emissive to absorptive signals appears to be twice as large in a magnetic field of 1.4 T compared to the ratio in spectra acquired at 2.4 T. If the contributions from the DD and TSM mechanisms remain the same when decreasing the field strength, the enhancement factor for R26 RCs at 1.4 T can be estimated as 80000. This is a lower limit, since our simulations (*vide infra*) indicate that the contribution from the DD and TSM mechanisms decreases between 2.4 and 1.4 T.

The photo-CIDNP results indicate that for the lowest fields indeed contributions from the DR mechanism are very strong and dominate over the TSM and DD processes. This gives rise to the opportunity of characterizing the spin

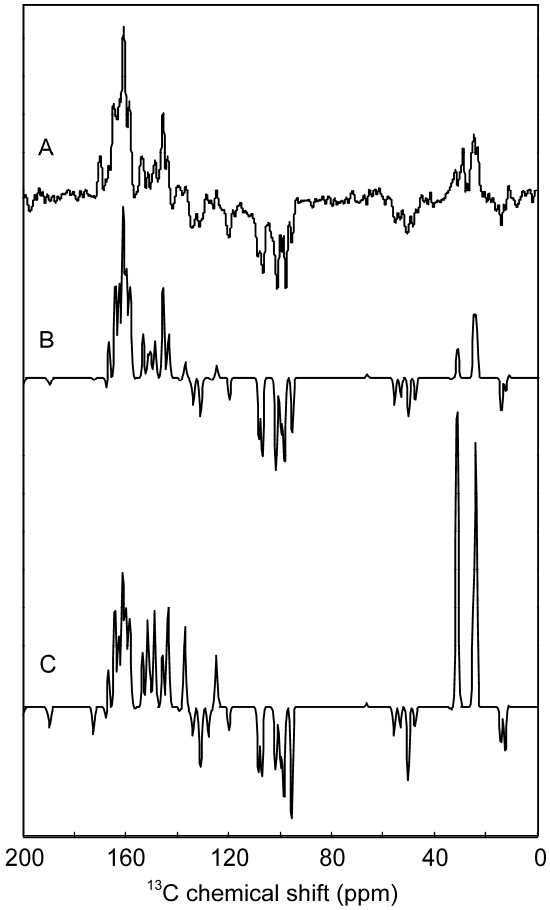

Figure 3.6: ^{13}C photo-CIDNP MAS NMR spectrum of *Rb. sphaeroides* R26 RCs in a magnetic field of 4.7 T immediately after a nanosecond laser flash[25] (A), fit obtained in matlab by scaling factors for simulated peak intensities (B) and simulation using the ΔA_k for the radical pair state from a DFT computation[5] (C).

density distribution for the triplet state of the special pair, ^{3}P. To do so, an estimate of the nuclear polarization generated by the RPM in the singlet and triplet branch with opposite signs is required. In principle, such an estimate can be obtained from simulations. For this, experimentally unknown ^{13}C hyperfine parameters ΔA_k in the radical pair state are required, which can be estimated by density functional theory (DFT) computations.[4,5] This approach does, however, introduces uncertainty from errors in the DFT calculations, which are approximate.

Here, a different route is followed, where the RPM polarization pattern is taken from time-resolved photo-CIDNP MAS NMR experiments that allow to observe the spectrum immediately after a single photocycle has been initiated by a laser pulse.[25] At that time polarization from the singlet branch, *i.e.* from cofactors

in RCs that have returned to the ground state following decay from the S state, is selectively detected, as RCs in the triplet branch are still in a paramagnetic state which shifts and broadens the NMR signals beyond detection. We have performed a linear least squares fit of the spectrum of *Rb. sphaeroides* R26 RCs obtained immediately after the nanosecond flash at 4.7 T[25] in Matlab with lorentzian lines by scaling of nuclear polarization values that were obtained using ΔA_k estimates from a DFT-based computation (Figure 3.6). This provides a table representing the intensity profile for the RPM polarization signal that can serve as a template for simulations. We apply this profile in all further analysis, although strictly it applies only at 4.7 T. By comparing simulations with and without such scaling to the experimental spectra, it was confirmed that RPM polarization scaled by the experimentally derived intensity factors provides a better approximation at the other fields than the RPM polarization simulated directly from DFT-computed ΔA_k values.

To simulate polarizations from the DR mechanism, the nuclear longitudinal relaxation times $T_{1n,k}$ in the ^{3}P state are required. In a first exploration of the DR mechanism,[46] McDermott *et al.* used a uniform *ad hoc* relaxation time of 300 s^{-1} to fit ^{15}N photo-CIDNP MAS NMR data. In contrast with this earlier simplified treatment, I find that it is possible to use the powder-averaged Redfield theory expression

$$T_{1n,k} = 45\ \omega_I^2\ T_{1T}/\ (4\Delta A_k^2) \qquad (3.1)$$

as well, as a first approximation, where $\Delta A_k = 3(A_{z,k} - a_{iso,k})/2$ is the hyperfine anisotropy of nucleus k, ω_I is the nuclear Zeeman frequency, which scales linearly with the magnetic field, and T_{1T} is the longitudinal electron spin relaxation time in the ^{3}P state.* The z-axis is here again along the principal component with the largest magnitude. Eq. (3.1) can be obtained from an expression for the paramagnetic relaxation in solids derived by Abragam[27], by replacing the distance-dependent dipole-dipole coupling between electron and nuclear spin by the ΔA_k which is

* Eq (3.1) matches Abragam's definition $\Delta A = 3\gamma_I^2\gamma_S^2\nabla^2\mu_0^2/(16\pi^2 r^6)$ for the point-dipole approximation. This expression is a factor of three smaller than the convention used in this chapter, and because the square of ΔA is used, a factor of 9 is introduced in the numerator of Eq. (3.1) relative to the existing literature.[27]

Cofactor	Atom number	ΔA_k ^{13}C hfi anisotropy [MHz]
P_L	1	8.8
	2	12.7
	3	3.8
	3'	0.6
	4	9.3
	5	1.8
	6	8.7
	9	10.6
	10	2.7
	11	9.7
	12	15.1
	13	3.1
	13'	1.2
	14	7.9
	15	5.2
	16	13.0
	19	10.2
	20	5.8
P_M	1	6.2
	2	9.8
	3	2.5
	4	5.8
	5	2.9
	6	4.9
	9	7.0
	10	4.5
	11	6.5
	12	12.1
	13	2.1
	13'	1.2
	14	5.8
	15	3.0
	16	7.5
	19	6.3
	20	3.8

Table 3.1. Hyperfine anisotropies ΔA_k for the ^{13}C nuclei in the L and M moieties computed by DFT with the BLYP functional.

largely due to spin density in p_z orbitals, and assuming $|\omega_I T_{1T}| >> 1$, which applies for all magnetic fields used in this work.

From measurements of T_{1T} in *Rb. sphaeroides* R26 RCs along the Y axis of the zero-field splitting tensor at a temperature of 233 K and a field of

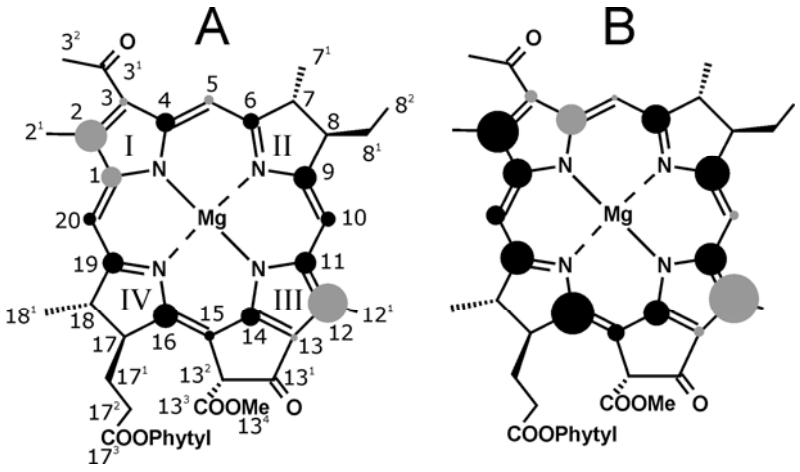

Figure 3.7. Spin density distribution in the special pair triplet state visualized via the relative anisotropic hyperfine parameter ΔA_k for the ^{13}C nuclei computed by DFT with the BLYP functional in the M (A) and L (B) moiety. Atom numbering is shown in (A). A circle diameter of one carbon-carbon bond length corresponds to $\Delta A_k = 2\pi \cdot 15$ MHz. Black circles correspond to hyperfine anisotropies that can be experimentally tested, while gray circles indicate the hyperfine anisotropies that are not accessible experimentally.

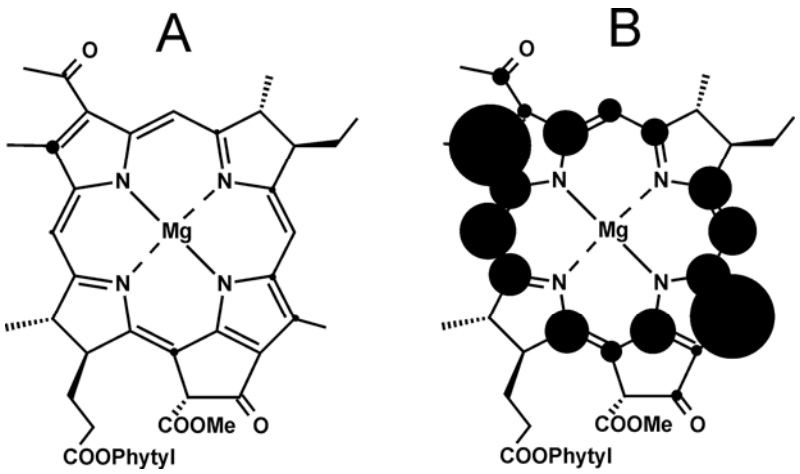

Figure 3.8: Spin density distribution in the special pair triplet state visualized via relative anisotropic ^{13}C hyperfine parameters ΔA_k computed by DFT with the BP86 functional in the M (A) and L (B) moiety. The atom numbering is same as in Figure 3.6 A. A circle diameter of one carbon-carbon bond length corresponds to $\Delta A_k = 2\pi \cdot 15$ MHz.

approximately 0.35 T,[47] we expect that T_{1T} is in the microsecond range. Our DFT computations show that the ΔA_k for the nuclei with the largest spin density are of the order of $2\pi \cdot 10$ MHz (Table 3.1). The Redfield regime normally breaks down

when $T_{1T} \sim 3/\Delta A_k$ and is violated for T_{1T} larger than ~ 20 ns. However, the scaling with ΔA_k^2 is expected to hold for $\Delta A_k << 2\ \omega_I$, *i.e.* up to ~ 10 T as in this regime second order perturbation theory, as simplified in Redfield theory, provides a good approximation.[27] In addition, preliminary computations for electron spin 1/2 indicate that the Redfield approximation remains valid throughout the range of T_{1T} and ΔA_k encountered in this work (data not shown). Since Redfield theory is semi classical, it is applicable to spin 1 electronic systems as well.

Estimates for the ΔA_k in Eq. (3.1) were obtained by two DFT computations for the triplet state of the special pair. The first computation, used already in [5] was based on non-optimized heavy atom coordinates of the x-ray crystal structure of R26 RCs in the charge neutral state (PDB 1AIJ).[40] Protons were attached with standard bond lengths and geometries and a spin-unrestricted computation with the BLYP functional was performed.[38,39] This leads to a spin density that is almost symmetrically distributed over the two moieties of the special pair, with only a

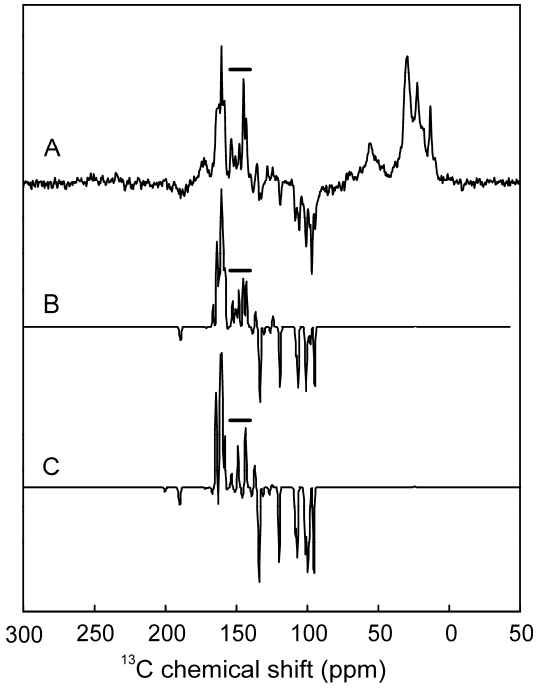

Figure 3.9. ^{13}C MAS NMR spectrum of quinone depleted RCs of *Rb. sphaeroides* R26 under illumination at 4.7 T (A) as well as numerical simulations of the photo-CIDNP effect with T_{1T} = 56 ns and triplet spin density from DFT computations with the BLYP functional (B) and the BP86 functional (C). The bars denote a spectral range where the number of signals differs in the two simulations.

slight excess in the L moiety (Figure 3.7). In the second DFT computation the WT special pair structure was optimized in TURBOMOLE[48] first for the radical cation state and then for the triplet state and the ΔA_k were obtained by a spin-unrestricted computation with the BP86 functional.[38,49] This led to a completely asymmetrical spin density distribution with both unpaired electrons being localized almost exclusively on the L moiety (Figure 3.8).

Nuclear polarization after a single photocycle for R26 RCs for the singlet branch ($p_{S,k}$) and triplet branch ($p_{T,k}$) due to RPM, and the TSM and DD mechanisms was computed by the density operator formalism, following the procedures described in reference [5]. Polarization p_k after return of molecules from both branches to the ground state was taken as an approximation for the steady-state polarization observed in our experiments. This is computed by

$$p_k = p_{S,k} + [1 - \exp(-\tau_T/T_{1n,k})]\, p_{T,k} \qquad (3.2)$$

where τ_T is the triplet lifetime (100 μs for R26 and 0.1 μs for WT RCs) and the $T_{1n,k}$ are calculated by Eq. (3.1). For every spectrum T_{1T} in Eq. (3.1) is the only fit parameter. Finally, the p_k are multiplied by the experimental RPM scaling factors

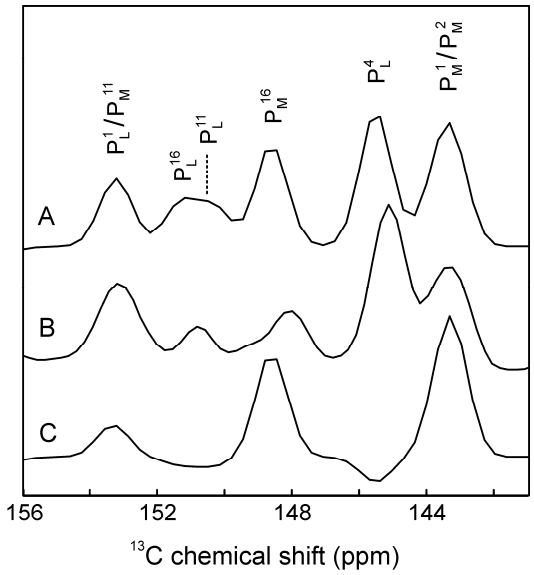

Figure 3.10. Detail of the ^{13}C photo-CIDNP MAS NMR spectrum of quinone depleted RCs of *Rb. sphaeroides* R26 obtained with continuous illumination in a magnetic field of 9.4 T (A), as well as numerical simulations of the photo-CIDNP effect with T_{1T} = 56 ns and triplet spin density from DFT computations with the BLYP functional (B) and the BP86 functional (C).

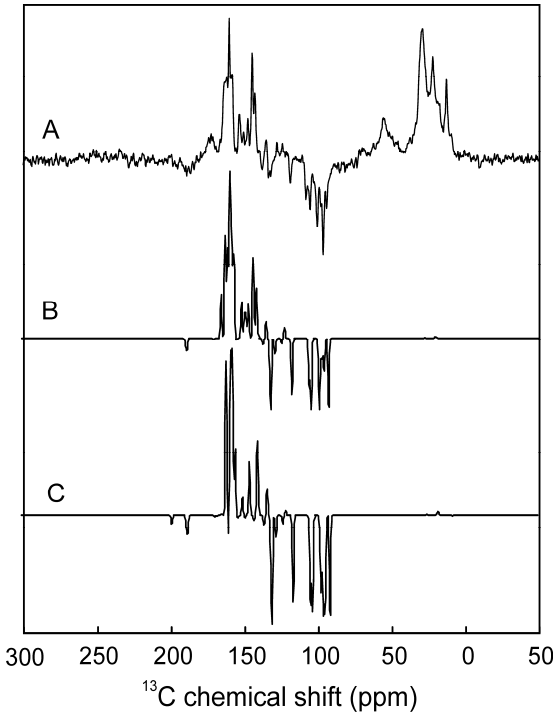

Figure 3.11: ^{13}C MAS NMR spectrum of quinone depleted RCs of *Rb. sphaeroides* R26 obtained with continuous illumination in a magnetic field of 9.4 T (A), as well as numerical simulations of the photo-CIDNP effect with T_{1T} = 0.5 μs and triplet spin density from DFT computations with the BLYP functional (B) and the BP86 functional (C).

that were obtained by fitting the time-resolved photo-CIDNP MAS NMR data collected at 4.7 T and shown in figure 3.6. Figure 3.9 shows the analysis of the data collected at 4.7 T. The best fit for both sets of ΔA_k with T_{1T} = 56 ns is obtained here. Well in line with earlier investigations, the agreement between experiment and simulation is better for the BLYP computation without geometry optimization of the R26 structure (Figure 3.9 B) than for the BP86 computation after geometry optimization of the WT structure (Figure 3.9 B). In particular, in the chemical shift range between 141 and 156 ppm (overbars) the number of signals differs between the two simulations and only the BLYP simulation agrees with experiment.

The analysis of the data collected in a magnetic field of 9.4 T confirm that T_{1T} = 56 ns over a considerable field range. From the detail plot shown in Figure 3.10 it is clear that signals from both moieties are experimentally observed with similar intensity, as is predicted by the BLYP computation without geometry optimization of the R26 structure, but not by the BP86 simulation with geometry optimization of the WT structure (see Figure 3.11 for simulation of the complete

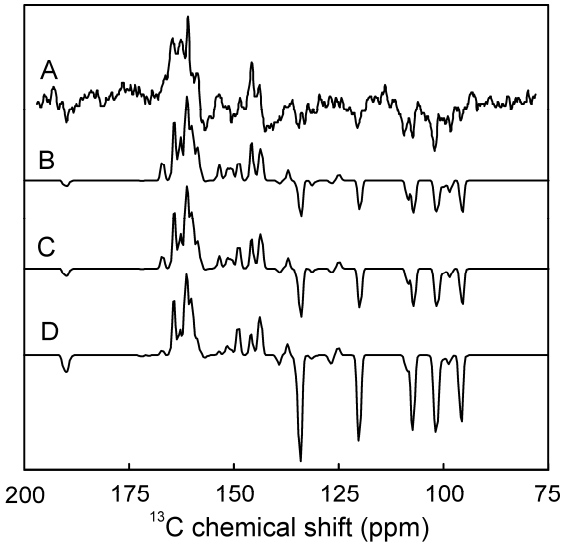

Figure 3.12. Detail of the ^{13}C MAS NMR spectrum of quinone depleted RCs of *Rb. sphaeroides* R26 under illumination in a magnetic field of 17.6 T (A) as well as numerical simulations of the photo-CIDNP effect triplet spin density using the ΔA_k from DFT computations with the BLYP functional at T_{1T} = 56 ns. (B), T_{1T} =22 ns (C) , and T_{1T} = 11 ns (D).

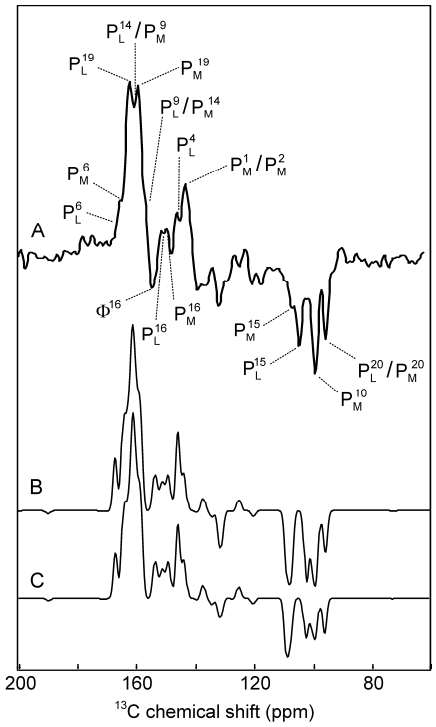

Figure 3.13 Detail of the ^{13}C MAS NMR spectrum of quinone depleted RCs of *Rb. sphaeroides* R26 under illumination in a magnetic field of 2.4 T (A) as well as numerical simulations of the photo-CIDNP effect triplet spin density from DFT computations with the BLYP functional at T_{1T} = 56 ns (B) and T_{1T} = 222 ns (C). To enhance the resolution for peak assignment, the experimental spectrum was subjected to a line-narrowing Lorentz-Gauss transformation.

spectrum). Simulation of the ^{13}C photo-CIDNP MAS NMR spectrum of R26 RCs at 17.6 T with the same T_{1T} = 56 ns that led to the best fits at 4.7 and 9.4 T results in an overestimate of the emissive signal intensity compared to the enhanced absorptive intensity (compare the spectra A and D in Figure 3.12). At this field the best overall fit quality is obtained with T_{1T} between 11 and 22 ns (spectra B and C). At the lowest field where a decoupled spectrum is obtained (2.4 T), the relative peak intensities depend rather weakly on T_{1T} (Figure 3.13). This is because already at T_{1T} = 222 ns (C) the prefactor $1-\exp(-\tau_T/T_{1n,k})$ in Eq. (2) is close to zero for most nuclei with significant RPM intensity. The fit quality only slightly improves for T_{1T} = 111 ns (not shown) and 56 ns (B) and degrades again towards shorter T_{1T}.

In contrast, in simulations of the WT spectra with τ_T = 100 ns for a magnetic field of 2.4 and 1.4 T, a marked dependence of the signal strength on T_{1T} in that range is detected (Figure 3.4). Due to the inverse square dependence of the relaxation rate $1/T_{1n,k}$ implied by Eq. (3.1), nuclear spin relaxation in the triplet branch can potentially become significant at such fields, even for the short-lived triplet state in WT RCs. For WT RCs, T_{1T} as short as 56 ns can be excluded at 1.4 T. Considering the relatively poor signal-to-noise ratio of these spectra, any $T_{1T} \geq 100$ ns provides acceptable fits and only a lower limit of T_{1T} is derived, although line shapes slightly change at longer T_{1T}.

For simulations of the field dependence of polarization due to the DR mechanism, an ad hoc power law $T_{1T} = 22.2 \cdot (17.6\ \mathrm{T}/B_0)^{0.69}$ ns was used, where B_0 is the magnetic field. The prefactor and exponent were chosen to provide a good match with the T_{1T} values at 17.6 and 4.7 T. This empirical choice fits all R26 spectra (Figure 3.14) and the WT spectra at 1.4 and 2.4 T (Figure 3.15).

Due to the square dependence of the $T_{1n,k}$ on ω_I and thus B_0 implied by Eq. (3.1), the empirical power law for T_{1T} leads to a scaling factor of $B_0^2/B_0^{0.69} = B_0^{1.31}$ $T_{1n,k}$. According to Eq. (3.2), such shortening of the $T_{1n,k}$ with decreasing field in turn leads to $p_k = p_{S,k}$ at sufficiently low field. Under such conditions the full nuclear polarization due to the RPM would be maintained and the Kaptein sign rules for cage products would apply.[50]

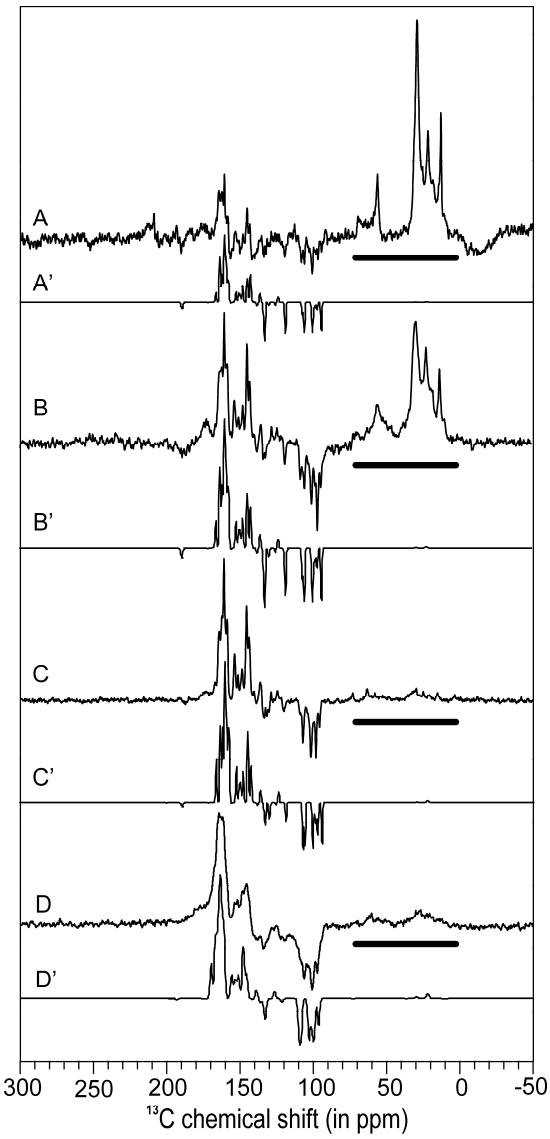

Figure 3.14: ^{13}C MAS NMR spectra of quinone depleted RCs of *Rb. sphaeroides* R26 with polarization enhancement by illumination in a magnetic field of 17.6 T (A), 9.4 T (B), 4.7 T (C), and 2.4 T (D) as well as numerical simulations of the photo-CIDNP effect with $T_{1T} = 0.2 \cdot (17.6\ \mathrm{T}/B_0)^{0.69}$ µs with triplet ΔA_k from a DFT computation with the BLYP functional without geometry optimization of the crystal structure at 17.6 (A'), 9.4 (B'), 4.7 (C'), and 2.4 (D') Tesla. The experimental data were obtained at 235 K with a MAS frequency of 8 kHz and using ^{1}H decoupling. Signals in the chemical shift range indicated by bars are present already in the dark.

The trend in nuclear polarization predicted from the simulations is in qualitative agreement with experimental observations (Figure 3.16 A). For WT RCs, maximum emissive polarization is expected around 4.7 T, while for the

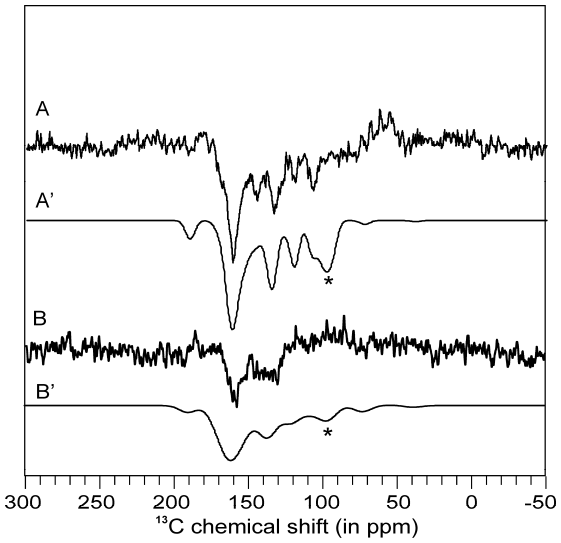

Figure 3.15: ^{13}C MAS NMR spectra of quinone depleted RCs of *Rb. sphaeroides* WT obtained by illumination in a magnetic field of 2.4 (A) and 1.4 (B) Tesla as well as numerical simulations of the photo-CIDNP effect with $T_{1T} = 0.2 \cdot (17.6\ \mathrm{T}/B_0)^{0.69}$ µs with triplet ΔA_k from a DFT computation with the BLYP functional without geometry optimization of the crystal structure for magnetic field strengths of 2.4 (A') and 1.4 (B') Tesla. The experimental data were obtained at a temperature of 235 K with a MAS frequency of 8 kHz and without ^{1}H decoupling. The asterisks denote methine carbon signals that are lost by broadening in spectra without decoupling.

polarization is very small at 1.4 T. The polarization in magnetic fields of 0.96, 0.48, and 0.24 T is also computed. These data points suggest that at even lower fields absorptive polarization due to the DR mechanism should appear. Note, however, that NMR sensitivity for a specific nuclear polarization scales with the square root of the magnetic field. If this scaling is taken into account, the maximum sensitivity in the low-field emissive spectra is expected to be about the same as for the absorptive spectra collected at 2.4 T and certainly worse than for the data obtained in a field of 4.7 T. Comparison of Figure 3.16 A and 3.17 A reveals that the emissive polarization in WT RCs in magnetic fields lower than 1.4 T in the *ad hoc* power law approach is due to the DR mechanism, since it vanishes at infinite T_{1T}.

For R26 RCs, the maximum nuclear polarization is predicted around 1.4 T, although the sensitivity for the same line width may be slightly better at 2.4 T (Figure 3.16 B). The contribution of acceptor signals to the maximum polarization corresponding to the blue dashed line, is comparable to the emissive donor signals at 4.7 T and much smaller than the donor signals at 2.4 and 1.4 T. For the field

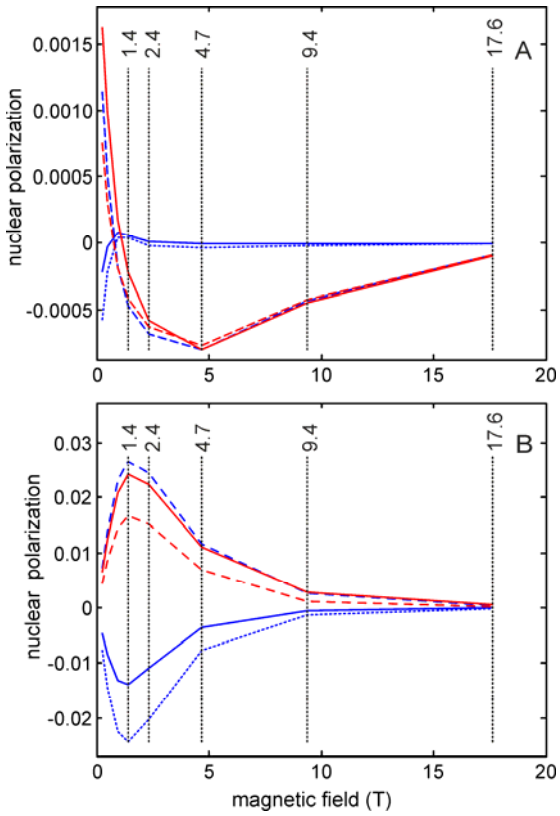

Figure 3.16. Simulated field dependence of donor nuclear polarization for selected nuclei of WT (A) and R26 (B) RCs of *Rb. sphaeroides*, with $T_{1T} = 22.2 \cdot (17.6\ \mathrm{T}/B_0)^{0.69}$ ns and triplet ΔA_k from a DFT computation with the BLYP functional without geometry optimization of the crystal structure. Blue lines correspond to the L moiety, P_L^4 solid line, P_L^{14} dashed, P_L^{15} dotted. Red lines correspond to the M moiety. P_M^{10} solid, P_M^{16} dashed. Black dotted vertical lines denote fields were measurements were performed.

dependence of acceptor nuclear polarization due to the TSM and DD mechanisms, see Figure 3.17 B.

A quantitative comparison of the experimental and simulated field dependence of the signal intensity is hampered by the fact that the experimental intensities at low fields cannot reliably be normalized. Signal-to-noise ratio for the reference signal in the dark spectrum is poor already at 4.7 T, very poor at 2.4 T, and the signal is not detected in the spectrum without decoupling at 1.4 T.

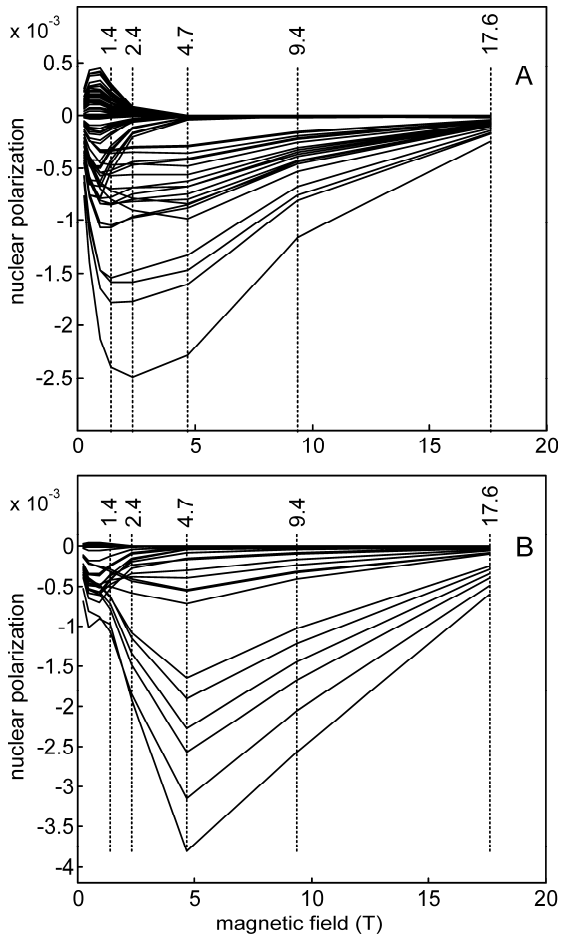

Figure 3.17. Simulated field dependence of donor nuclear polarization in the absence of differential relaxation, *i.e.*, for infinite T_{1T}, (A) and acceptor nuclear polarization (B) for RCs of *Rb. sphaeroides*. Dashed vertical lines denote fields where measurements are performed. Since neither of these simulations depends significantly on the triplet state lifetime τ_T, they apply to both R26 and WT RCs.

3.5 *Discussion*

3.5.1 *Triplet spin densities*

The conclusions on the electronic structure of the special pair triplet depend on the scaling of nuclear longitudinal relaxation times with the ΔA_k^2 suggested by the Redfield-regime expression in Eq. (3.1). The condition $\Delta A_k << 2\ \omega_I$ for the simplified Redfield theory is valid at 9.4 T, with $2\omega_I/\Delta A_k > 12$ for all nuclei. Hence, the data shown in Figure 3.10 provide convincing evidence for an approximately

symmetric distribution of spin density over the two moieties of the special pair, as opposed to a strongly biased one.

The slightly asymmetric spin density distribution suggested in Figure 3.7 on the basis of a DFT computation is in line with the experimental data. Observation of the DR effect, and thus any conclusion on a ΔA_k in the triplet state, depends on significant RPM polarization for this nucleus. This in turn requires at least a moderate hyperfine coupling of this nucleus in the radical pair state. This condition is fulfilled for all nuclei whose signals are assigned in Figure 3.10 or 3.13. The corresponding circles for the ΔA_k in the triplet state are shown in black in Figure 3.7. For the nuclei where these circles are shown in gray, the corresponding CIDNP signal was not yet identified and hence, no experimental information on the ΔA_k is available.

Given the uncertainties in estimating T_{1T} (*vide supra*) and the remaining differences between experimental data and DFT simulations of the spectra, the hyperfine anisotropies ΔA_k listed in Table 3.1 should be considered as approximate. However, the distribution implied by the black circles in Figure 3.7 is expected to be semi-quantitatively correct, since spin dynamics is very sensitive to relative hyperfine couplings within the field range of more than one order of magnitude that is studied here, and the agreement between experiment and simulation is good throughout this field range (Figure 3.14).

In a simple picture, the electron spin density of the ^{3}P state can be rationalized in terms of a linear combination of a single-electron occupied HOMO and a single-electron occupied LUMO. Since the electron spin density in the radical cation state, which is related to the HOMO, has been demonstrated to be shifted to the L cofactor[4,25,51], our data suggest that the LUMO is somewhat shifted to the M cofactor. This is in line with results from Stark spectroscopy[52,53] and the tentative interpretation of results from ^{1}H ENDOR spectroscopy on ^{3}P.[54,23] In Figure 3.7, the gray circles correspond to atoms that should have significant LUMO electron density and small HOMO electron density.

3.5.2 *Longitudinal relaxation times of the nuclei and of the electron spin in the donor triplet state.*

The empirical power law $T_{1T} = 22.2 \cdot (17.6\ \mathrm{T}/B_0)^{0.69}$ ns, together with the Redfield-regime expression, Eq. (3.1), provide a good global fit of the photo-CIDNP data over more than one order of magnitude variation in the external magnetic field and qualitative agreement with the observed trends in signal intensity for R26 and WT RCs. The longitudinal relaxation times of the electron spins in the donor triplet predicted by Eq. 3.1 at a nominal temperature of 235 K are within an order of magnitude of the T_{1T} measured at 0.35 T by Hoff *et al.* along the *y* direction of the zero-field splitting tensor at 233 K.[47] This answers the long standing question[46] whether the DR mechanism in the solid state, as originally suggested by Goldstein and Boxer,[22] is a consistent explanation for the enhanced absorptive signals observed in *Rb. sphaeroides* R26 photosynthetic RCs.

3.5.3 *Field dependence of the solid-state photo-CIDNP mechanisms*

For photosynthetic RCs of the carotenoid-less R26 strain of *Rb. sphaeroides*, maximum polarization enhancement by the DR mechanism appears predominant at low field and occurs at lower fields than for the TSM and DD mechanisms. In addition, the optimum field for DR enhancement in WT RCs is lower than for R26.

For practical applications, the optimum field for polarization enhancement depends on the information that one seeks in the NMR spectra. If chemical shift assignments and magnetic parameters in the paramagnetic states with atomic resolution are requested, values of signal-to-noise ratio have to be compared at the same chemical shift resolution. This is possible, since in any spectroscopy sensitivity can be traded for resolution by deconvolution-convolution techniques, as they are applied to the spectrum shown in Figure 3.13. In this case, polarization enhancement for R26 RCs with dominating DR effect is optimal at fields between 4.7 and 9.4 T.

In other cases it may be sufficient to detect and roughly assign the polarization enhanced signals. Sensitivity is then proportional to $pB_0^{1/2}$, where p is the nuclear polarization. For R26 RCs, the optimum is then achieved at fields between 1.4 and 2.4 T.

Polarization enhancement with respect to thermal equilibrium polarization scales with p/B_0 because thermal equilibrium polarization in the high temperature approximation linearly scales with the transition frequency and thus with B_0. This parameter increases with decreasing field for all nuclei within the whole field range $B_0 > 0.25$ T that is simulated. Note however that the field dependence of this enhancement is of practical relevance only if contrast between polarization enhanced and thermal equilibrium signals needs to be optimized.

3.5.4 *Photo-CIDNP MAS NMR as enhancement method for solid-state NMR*

It is already shown here that the high-field TSM and DD mechanisms acting in RCs of *Rb. sphaeroides* show -as it is expected for a mechanism based on a matching condition[2]- a maximum, which is around 2 T. The maximum effect might well be encountered at lower fields for other electron transfer systems which may have weaker ^{13}C hyperfine couplings or smaller g value differences. In fact, the only observation of the solid-state photo-CIDNP effect in a non-photosynthetic system, a mutated blue-light photoreceptor, (see chapter 4) was achieved in a relatively low field of 2.4 T. Hence, application of lower fields might be a key to develop photo-CIDNP MAS NMR based on TSM and DD into a more generally applicable method for signal enhancement in solid-state NMR.

The main difficulty with such an approach is a loss of chemical shift resolution at lower fields, which is equivalent to a loss in effective sensitivity (*vide supra*). This problem could be circumvented by polarizing at lower fields than detecting, which requires shuttling of the sample between regions of the magnet with different field.[55,56] General application of solid-state photo-CIDNP would require artificial electron transfer systems which could be applied to surfaces and cavities in 'spin-torch' experiments in which the photo-CIDNP is transferred to explore the environment.

The simulations indicate that much stronger nuclear polarization can be obtained with optimized DR conditions than for the TSM and DD mechanisms (Figure 3.16). This is plausible, since the TSM and DD mechanisms depend on electron-nuclear spin state mixing near an avoided level crossing, which cannot be optimized for all nuclei at the same time and for a second matching condition,

which cannot be controlled. This second matching is between the time scales of radical pair decay and hyperfine evolution for the DD mechanism or the electron Zeeman difference frequency and nuclear Zeeman frequency for the TSM mechanism.

In contrast, the DR mechanism depends on RPM polarization, which can lead to values of p of the order of unity. This polarization is completely retained in the ground state if nuclear spin longitudinal relaxation in the triplet state is much faster than triplet decay. The simulations demonstrate that this situation can be attained for many nuclei in R26 RCs at fields lower than 2.4 T. Hence, it appears feasible to achieve high absolute polarization of several percent also for artificial systems.

References

(1) Zysmilich, M. G.; McDermott, A. *J. Am. Chem. Soc*. **1994**, *116*, 8362-8363.

(2) Jeschke, G.; Matysik, J. *Chem. Phys.* **2003***, 294***,** 239-255.

(3) Daviso, E.; Jeschke, G.; Matysik, J. in *Biophysical Techniques in Photosynthesis II* (Aartsma T.J., Matysik, *J., eds.), Springer Dordrecht, pp. 385-399* (2008).

(4) Prakash, S.; Alia; Gast, P.; de Groot, H. J. M.; Jeschke, G.; Matysik, J. *J. Am. Chem. Soc.* **2005**, *127*, 14290-14298.

(5) Prakash, S.; Alia; Gast, P.; de Groot, H. J. M.; Matysik, J.; Jeschke, G. *J. Am. Chem. Soc.* **2006**, *128*, 12794-12799.

(6) Janssen, G. J.; Daviso, E.; van Son, M.; de Groot, H. J. M.; Alia, A.; Matysik, J. *Photosynth. Res.* **2010**, *104*, 275-282.

(7) Matysik, J.; Alia, Gast, P.; van Gorkom, H. J.; Hoff, A. J.; de Groot. H. J. M. *Proc. Natl. Acad. Sci. USA*. **2000**, *97*, 9865-9870.

(8) Alia; Roy, E.; Gast, P.; van Gorkom, H. J.; de Groot, H. J. M.; Jeschke, G.; Matysik, J. *J. Am. Chem. Soc.* **2004**, *126*, 12819-12826.

(9) Diller, A.; Roy, E.; Gast, P.; van Gorkom, H. J.; de Groot, H. J. M.; Glaubitz, C.;Jeschke, G.; Matysik, J. Alia, A. *Proc. Natl. Acad. Sci. U. S. A*. **2007**, *104*, 12767-12771.

(10) Roy, E., Alia, Gast, P.; van Gorkom, H. J.; de Groot, H. J. M.; Jeschke, G.; Matysik, J. *Biochem. Biophys. Act.* **2007**, *1767*, 610–615.

(11) Roy, E.; Rohmer, T.; Gast, P.; Jeschke, G.; Alia, A.; Matysik, J. *Biochemistry* **2008**, *47*, 4629-4635.

(12) Matysik, J.; Diller, A.; Roy, E.; Alia, A. *Photosynth. Res.* **2009**, *102*, 427-435.

(13) Daviso, E.; Alia, A.; Prakash, S.; Diller, A.; Gast, P.; Lugtenburg, J.; Jeschke, G.; Matysik, J. *J. Phys. Chem. C* **2009**, *113*, 10269-10278.

(14) Hoff, A. J.; Deisenhofer, J. *Phys. Rep.* **1997**, *287*, 2-247.

(15) Hunter, C. N.; Daldal, F.; Thurnauer, M. C.; Beatty, J. T. *The Phototropic Purple Bacteria* in *Advances in Photosyntheis and Respiration* (Series editor Govindjee)*, Springer Dordrecht, Volume 28* (2008).

(16) Jeschke*,* G. *J. Chem. Phys.* **1997**, *106*, 10072-10086.

(17) Jeschke, G. *J. Am. Chem. Soc.* **1998**, *120*, 4425-4429.

(18) Polenova, T.; McDermott, A. E. *J. Phys. Chem. B.* **1999**, *103*, 535-548.

(19) Closs, G. L.; Closs, L. E. *J. Am. Chem. Soc*. **1969**, *91*, 4549-4550.

(20) Kaptein, R.; Oosterhoff, J. L. *Chem. Phys. Lett*. **1969**, *4*, 195-197.

(21) Closs, G. L. *Chem. Phys. Lett*. **1975**, *32*, 277-278.

(22) Goldstein, R. A.; Boxer, S. G. *Biophys. J*. **1987**, *51*, 937-946.

(23) Marchanka, A.; Paddock, M.; Lubitz, W.; van Gastel, M. *Biochemistry* **2007**, *46*, 14782-14794.

(24) Marchanka, A.; Savitsky, A.; Lubitz, W.; Möbius, K.; van Gastel, M. *J. Phys. Chem. B* **2010**, *114*, 14364-14372.

(25) Daviso, E.; Prakash, S.; Alia, A.; Gast, P.; Neugebauer, J.; Jeschke, G.; Matysik, J. *Proc. Natl. Acad. Sci. USA*. **2009**, *106*, 22281-22286.

(26) Diller, A.; Prakash, S.; Alia, A.; Gast, P.; Matysik, J.; Jeschke, G. *J. Phys. Chem. B*. **2007**, *111*, 10606-10614.

(27) Abragam, A. *Principles of Nuclear Magnetism*, *Oxford University Press*, (1962).

(28) Jeschke, G.; Anger, B. C.; Bode, B. E.; Matysik, J. *J. Phys. Chem. A*. **2011**, *115*, 9919-9928.

(29) Shochat, S.; Arlt, T.; Francke, C.; Gast, P.; Vannoort, P. I.; Otte, S. C. M.; Schelvis, H. P. M.; Schmidt, S.; Vijgenboom, E.; Vrieze, J.; Zinth, W.; Hoff, A. J. *Photosyn. Res.* **1994**, *40*, 55-66.

(30) Feher, D.; Okamura, M. Y. In *The Photosynthetic Bacteria;* Clayton, R. K., Siström, W., Eds.; Plenum Press: New York, 1978; p 349-378.

(31) Okamura, M. Y.; Isaacson, R. A.; Feher, G. *Proc. Natl. Acad. Sci. U.S.A.* **1975**, *72*, 3491-3495.

(32) Fischer, M. R.; de Groot, H. J. M.; Raap, J.; Winkel, C.; Hoff, A. J.; Lugtenburg, J. *Biochemistry* **1992**, *31*, 11038-11049.

(33) Bennett, A. E.; Rienstra, C. M.; Auger, M.; Lakshmi, K. V.; Griffin, R. G. *J. Chem. Phys.* **1995**, *103*, 6951-6958.

(34) Zhang, S.; Wu, X.; Mehring, M. *Chem. Phys. Lett.* **1990**, *173,* 481-484.

(35) Matysik, J.; Alia; Hollander, J. G.; Egorova-Zachernyuk, T.; Gast, P.; de Groot, H. J. M. *Indian J. Biochem. Biophys.* **2000**, *37*, 418-423.

(36) te Velde, G.; Bickelhaupt, F. M.; van Gisbergen; S. J. A.; Fonseca Guerra, C.; Baerends, E. J.; Snijders, J. G.; Ziegler, T. J. Comput. Chem. 2001, 22, 931.

(37) ADF2004.01, SCM, Theoretical Chemistry, Vrije Universiteit, Amsterdam, The Netherlands, http://www.scm.com

(38) Becke, A. D. *Phys. Rev. A* **1988**, *38*, 3098.

(39) Lee, C.; Yang, W.; Parr, R. G. *Phys. Rev. B* **1988**, *37*, 785.

(40) Stowell, M. H.; McPhillips, T. M.; Rees, D. C.; Soltis, S. M.; Abresch, E.; Feher, G. *Science* **1997**, *276*, 812-816.

(41) ADF2009.01, SCM, Theoretical Chemistry, Vrije Universiteit, Amsterdam, The Netherlands, http://www.scm.com

(42) Dunning, T. H. Jr. *J. Chem. Phys.***1989**, *90*, 1007.

(43) Ermler, U.; Fritzsch, G.; Buchanan, S. K.; Michel, H. *Structure* **1994**, *2*, 925-936.

(44) Eichkorn, K.; Treutler, O.; Öhm, H.; Haser, M.; Ahlrichs, R. *Chem. Phys. Lett.* **1995**, *242*, 652.

(45) Eichkorn, K.; Weigend, F.; Treutler, O.; Ahlrichs, R. *Theor. Chem. Acc.* **1997**, *97*, 119.

(46) McDermott, A.; Zysmilich, M. G.; Polenova, T. *Solid State Nuc. Magn. Reson.* **1998**, *11*, 21-47.

(47) Hoff, A. J.; Proskuryakov, I. I. *Chem. Phys. Lett.* **1985**, *115*, 303-310.

(48) Ahlrichs, R.; Bär, M.; Häser, M.; Horn, H.; Kälmel, C. *Chem. Phys. Lett.* **1989**, *162*, 165.

(49) Perdew, J. P.; Wang, Y. *Phys. Rev. B* **1986**, *33*, 8822.

(50) Kaptein, R. *J. Chem. Soc. Chem. Commun.* **1971**, 732-733.

(51) Lendzian, F.; Huber, M.; Isaacson, R. A.; Endeward, B.; Plato, M.; Bönigk, B.; Möbius, K.; Lubitz, W.; Feher, G. *Biochim. Biophys. Acta* **1993**, *1183*, 139-160.

(52) Lockhart, D. J.; Boxer, S. G. *Proc. Natl. Acad. Sci. U. S. A.* **1988**, *85*, 107-11.

(53) Moore, L. J.; Zhou, H.; Boxer, S. G. *Biochemistry* **1999**, *38*, 11949-60.(54) Lubitz, W.; Lendzian, F.; Bittl, R. *Acc. Chem. Res.* **2002**, *35*, 313-320.

(55) Grosse, S.; Gubaydullin, F.; Scheelken, H.; Vieth, H. M.; Yurkovskaya, A. V. *Appl. Magn. Reson.* **1999**, *17*, 211-225.

(56) Ivanov, K. L.; Miesel, K.; Yurkovskaya, A. V.; Korchak, S. E.; Kiryutin, A. S.; Vieth, H. M. *Appl. Magn. Reson.* **2006**, *30*, 513-534.